Robotic Rotational Positioning of End-Effectors for Micromanipulation

Songlin Zhuang, *Member, IEEE*, Changsheng Dai, *Member, IEEE*, Guanqiao Shan, *Graduate Student Member, IEEE*, Changhai Ru, Zhuoran Zhang, *Member, IEEE*, and Yu Sun, *Fellow, IEEE*

***Abstract*—Precise rotational positioning of end-effectors under microscopy is crucial for robotic micromanipulation. However, the end-effector is presently limited to a fixed orientation, which is manually set before a given micromanipulation task, lacking accuracy and versatility of *in situ* reorientation. In this article, we present a unified framework for rotationally positioning the end-effector in three dimensions by establishing a general rotational model, developing a detection method within the limited field of view under microscopy, and designing a three-loop control strategy that adapts to different experimental requirements and model parameters. In experiments, a standard angled micropipette was used as the end-effector to verify the validity of the proposed methods. The performance was evaluated experimentally where the micropipette was robotically rotated to an arbitrarily desired orientation with an average orientation error less than 2°. In the experiments of sperm manipulation, the *in situ* micropipette orientation control capability improved the success rate of sperm immobilization and achieved dexterous robotic sperm orientation for facile aspiration.**

***Index Terms*—Cell manipulation, end-effector, micromanipulation, rotational positioning.**

I. Introduction

ROBOTIC micromanipulation is used for manipulating biological samples in biomedical research and clinical applications, such as in vitro fertilization [1], patch clamp recording [2], cloning [3], and imaging [4]. It is desired to have the end-effector to possess the capability of rotational positioning for placing or orienting a sample. For instance, in intracytoplasmic sperm injection (ICSI), an angled micropipette tip must be aligned with the micropipette body to eliminate the misalignment error before sperm immobilization and oocyte injection [5] [see Fig. 1(a)]. For multidirectional imaging of a sample, 360° rotational positioning of the end of a robotic nanomanipulation system is required [6] [see Fig. 1(b)]. Fig. 1(c) shows that embryo deformation and penetration force can be reduced during zebrafish embryo injection when the injection micropipette rotates homocentrically [7]. Other micromanipulation applications that require rotational positioning of an end-effector can be found in [8]–[13].

These tasks can all boil down to the rotational positioning problem of end-effectors under microscopy where the rotational axis has a tilted angle to the focal plane of the microscope [see Fig. 1(d)]. Compared to the translational positioning under optical microscopy [14]–[17], rotating end-effectors can easily move the tip out of the field of view (FOV) and depth of focus

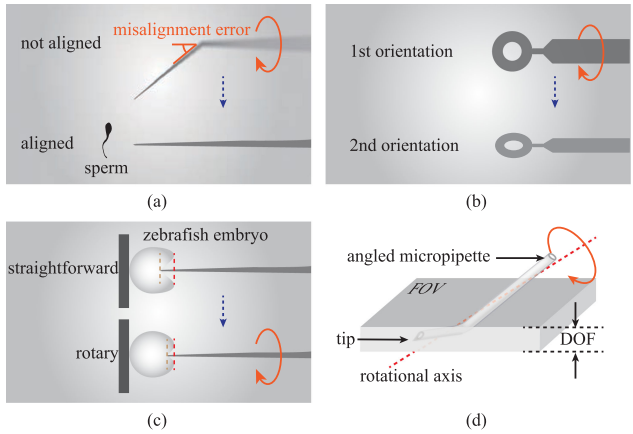

Fig. 1. Micromanipulation tasks that require rotational positioning of end-effectors under microscopy. (a) Misalignment error between the micropipette tip and the micropipette body must be eliminated before it taps the substrate for sperm immobilization [5]. (b) Different orientations of the sample attached to the end of a nanomanipulation system are required for 360° imaging [6]. (c) Rotary injection exerts lower damage than straightforward embryo injection [7]. (d) Class of general rotational positioning problems under microscopy where the rotational axis has a tilted angle to the microscope focal plane and the feature points (such as the end-effector's tip) are far from the rotational axis.

Manuscript received 6 July 2021; revised 21 October 2021; accepted 8 January 2022. Date of publication 3 February 2022; date of current version 8 August 2022. This work was supported in part by the Natural Sciences and Engineering Research Council of Canada (NSERC) via a Discovery Grant, in part by the Canada Research Chairs Program, and in part by the Ontario Research Fund via a Research Excellence Grant. This paper was recommended for publication by Associate Editor Yajing Shen and Editor Arianna Menciassi upon evaluation of the reviewers' comments. *(Songlin Zhuang and Changsheng Dai contributed equally to this work.) (Corresponding authors: Zhuoran Zhang; Yu Sun.)*

Songlin Zhuang is with the Research Institute of Intelligent Control and Systems, Harbin Institute of Technology, Harbin 150080, China, and also with the Department of Mechanical and Industrial Engineering, University of Toronto, Toronto, ON M5S 3G8, Canada (e-mail: songlin.zhuang@utoronto.ca).

Changsheng Dai, Guanqiao Shan, and Yu Sun are with the Department of Mechanical and Industrial Engineering, University of Toronto, Toronto, ON M5S 3G8, Canada (e-mail: changsheng.dai@mail.utoronto.ca; gq.shan@mail.utoronto.ca; sun@mie.utoronto.ca).

Changhai Ru is with the School of Electronic and Information Engineering, Suzhou University of Science and Technology, Suzhou 215009, China (e-mail: rchhai@163.com).

Zhuoran Zhang is with the School of Science and Engineering, The Chinese University of Hong Kong, Shenzhen 518172, China (e-mail: zhangzhuoran@cuhk.edu.cn).

This article has supplementary material provided by the authors and color versions of one or more figures available at https://doi.org/10.1109/TRO.2022.3142671.

Digital Object Identifier 10.1109/TRO.2022.3142671

(DOF). This problem becomes more challenging when the target points, such as the end-effector's tip or feature points on the sample, are far from the rotational axis. In this more general case, a very small rotation of the end-effector can induce large horizontal and vertical translation.

Presently, the rotational positioning of an end-effector under optical microscopy is manually performed. The drawbacks of manual operation include low accuracy and high risk of damage because the rotation of an end-effector changes the tip position and blurs the tip. It is difficult to handle these two problems particularly under high magnifications where the microscope's FOV is very limited.

Several techniques have been reported for robotic rotational positioning under microscopy. In [6], a triple-image alignment (TIA) approach was proposed to identify a kinematic rotational model, where the end-effector needs to be oriented to no less than three positions far from each other for calibration. In micromanipulation, the end-effectors, such as micropipettes, are frequently replaced; thus, model updates and recalibration are needed every time of end-effector change, making the TIA approach cumbersome to use. Additionally, the TIA approach yields large model errors when the end-effector's tip is far from the rotational axis (see Section VI-A). In [18], a double closed-loop servo repetitive controller was developed and achieved better rotational positioning results than the TIA approach, with the sacrifice of costing more time to identify the dynamic model. In [19], a PD controller was applied to axially rotate a zebrafish larva for the injection and imaging of different organs; however, this approach was only able to evaluate a limited number of orientations (e.g., ventral and dorsal) and cannot characterize 360° orientations. To date, no effective method exists for the challenging case where the end-effector's tip is far from the rotational axis. In another class of rotational positioning methods (e.g., [11], [20], [21]), the rotational axis is parallel to the microscope's optical axis; thus, the rotational motion of the actuators does not blur the image, which can be viewed as a particular case of our interest.

The challenges to overcome in this work include the following:

1) A model and metrics suitable for the general case in Fig. 1(d) that can characterize 360° orientations of the end-effector in three dimensions (3-D) are lacking.
2) The end-effector's tip is far from the rotational axis, and the axis has a tilted angle to the microscope's focal plane. In this general setup used in the majority of practical micromanipulation tasks, the end-effector's tip is easily moved out of the microscope's FOV and depth of field.
3) Recalibration after replacing an end-effector must be avoided to improve efficiency. Therefore, the developed control framework needs to be general and adaptive to uncertain model parameters.

We tackled these problems by establishing a general rotational model and defining the end-effector's orientations in 3-D; developing a detection method within the limited depth of field of a microscope and proposing the metrics of 360° orientations; designing a three-loop control framework that adapts to different environmental requirements and model parameters.

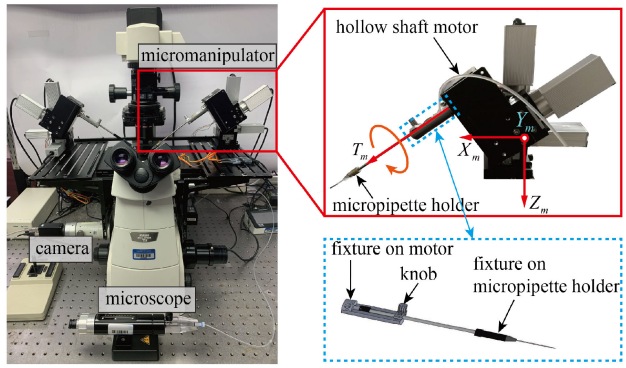

Fig. 2. General micromanipulation system setup that includes a micromanipulator and a camera attached to an inverted optical microscope. The micromanipulator has three translational axes X_m, Y_m, Z_m and an added rotational axis T_m.

To verify the validity of the technique, we integrate an angled rotational degree-of-freedom on a standard micromanipulator that only had translational degrees-of-freedom. We used a standard ICSI micropipette as the end-effector for testing because it has an angled tip far from the micropipette body which approximately coincides with the rotational axis. We tested the performance under 4× and 20× microscope objectives, and performed sperm immobilization and orientation under 20× microscope objective. The performance was demonstrated experimentally that the angled ICSI micropipette tip can be rotated to an arbitrarily desired orientation with an average orientation error of less than 2°. Moreover, the micropipette tip can always be maintained in a small region in the microscope's FOV center during orientation. The small region size (the average area ratios to the microscope's FOV are 0.6% and 0.04% under 4× and 20× microscope objectives, respectively) indicates the strong servo capability of the controllers. Sperm immobilization was performed after aligning the micropipette tip to the micropipette body. The success rate of immobilization was 98% under 20× microscope objective, significantly higher than that of 90% by manual alignment. Sperm orientation for aspiration was also achieved by dynamically rotating the micropipette tip to different orientations, which is difficult to achieve by human operators.

II. System Setup

The system is comprised of a standard micromanipulator (MX7600, Siskiyou) and a camera (scA1300-32gm, Basler) connected to an inverted optical microscope (Nikon Eclipse Ti-S), as shown in Fig. 2. The micromanipulator has three translational degrees-of-freedom (resolution: 0.1 μm along each axis). The camera captures images (resolution: 1200×900 pixels) at 30 frames per second. A standard ICSI micropipette (MIC-50-35, Origio) with an angled tip (35° to the micropipette body) for clinical use was mounted on the micromanipulator.

To enable the rotational positioning of the end-effector, a hollow shaft stepper motor (ST4118M1804-L, Nanotech) with positioning accuracy of 0.1125° was integrated to the micromanipulator such that it has three translational axes, denoted by X_m, Y_m, Z_m, and one rotational axis, denoted by T_m. A mechanical part was designed to mount on the central axis of

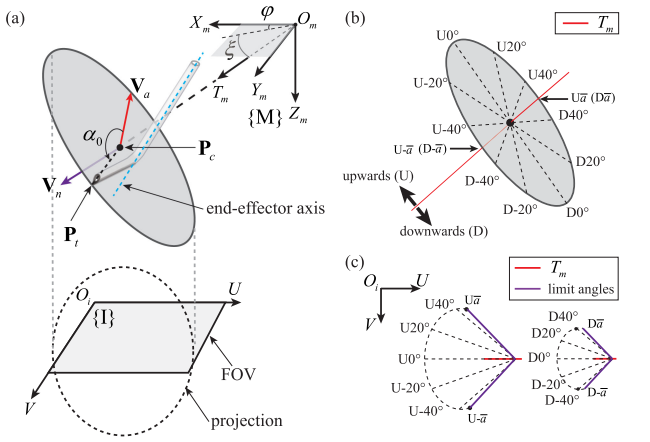

Fig. 3. General rotational model where the end-effector axis is not required to be collinear with the T_m axis, and the end-effector's tip is far from the T_m axis. (a) Relationships among the micromanipulator coordinate frame {M}, the tilted circle in 3-D, and the image plane coordinate frame {I}. (b) Definitions of 360° orientations in 3-D (side view). U$\pm\bar{a}$ and D$\pm\bar{a}$ are limit angles in upward and downward directions. (c) Misalignment angles of upward and downward directions in $O_i - UV$ (top view). 360° orientations in 3-D only correspond to a limited misalignment angle range $[-\bar{a}, \bar{a}]$, $\bar{a} \in [0, 360°]$.

the hollow shaft motor by the fixture on the micropipette holder. It has a structure of a hollow half-cylinder so that the central axes of the micropipette holder and the motor approximately coincide. This design facilitates safe and fast replacement of an end-effector by easily rotating a knob.

III. General Rotational Model

As illustrated in Fig. 3, the end-effector's tip rotates along a tilted circle in 3-D when the micromanipulator rotates about the T_m axis. Note that the end-effector axis is not required and not possible to be exactly collinear with the T_m axis due to machining and assembling errors. Existing rotational models can be considered as a particular case of our proposed model. For instance, if the T_m axis is parallel to the X_m axis, then rotation about the T_m axis does not move the end-effector's tip along the X_m axis; thus, our model reduces to the models in [6] and [18], which only involve Y_m, Z_m, and T_m axes. On the other hand, if the T_m axis is parallel to the Z_m axis, then our model reduces to the models in [11], [20], [21] where a rotary plate is installed under microscopy.

A tilted circle in 3-D can be represented by a parametric equation of α

$$\underbrace{\begin{bmatrix} p_x \\ p_y \\ p_z \end{bmatrix}}_{\mathbf{P}_t} = r\sin\alpha \left(\underbrace{\begin{bmatrix} \cos\xi\cos\varphi \\ \cos\xi\sin\varphi \\ \sin\xi \end{bmatrix}}_{\mathbf{V}_n} \times \underbrace{\begin{bmatrix} -\sin\varphi \\ \cos\varphi \\ 0 \end{bmatrix}}_{\mathbf{V}_a} \right) + r\cos\alpha \underbrace{\begin{bmatrix} -\sin\varphi \\ \cos\varphi \\ 0 \end{bmatrix}}_{\mathbf{V}_a} + \underbrace{\begin{bmatrix} p_{xc} \\ p_{yc} \\ p_{zc} \end{bmatrix}}_{\mathbf{P}_c}, \alpha \in [0, 2\pi] \quad (1)$$

where $\mathbf{P}_t$ denotes the end-effector's tip on the circle edge; r denotes the circle radius; α denotes the rotation angle within the circle plane; ξ denotes the included angle of T_m and $O_m - X_m Y_m$; φ denotes the included angle of X_m and the projection of T_m on $O_m - X_m Y_m$; $\mathbf{P}_c$ denotes the circle center. $\mathbf{V}_a$ and $\mathbf{V}_n$ are two orthonormal vectors used to characterize the circle's orientation in 3-D. The projection of the tilted circle in 3-D on $O_i - UV$ is an ellipse. Generally, only a small part of the ellipse appears in the microscope's FOV by rotating about the T_m axis for 360° under high magnifications. All the model parameters are marked in Fig. 3(a). The micromanipulator coordinate frame {M} involves X_m, Y_m, Z_m, and T_m axes. The image plane coordinate frame {I} involves U and V axes.

We define the misalignment angle by the included angle of the end-effector's tip and body in {I}. The misalignment angle, denoted by a_m, takes values in $[-\bar{a}, \bar{a}]$, where $\bar{a} \in [0, 360°]$ is a limit angle, i.e., an upper bound of misalignment angle depending on the system setup. In our system, the length of the ICSI micropipette tip is 400 μm. If $\xi = 35°$, then $\bar{a} \approx 40.5°$ by basic algebraic operations. Intrinsically, the misalignment angle is the projection of a 3-D angle on {I}; hence, one a_m corresponds to two orientations in the 3-D circle (except $\pm\bar{a}$). For instance, if $a_m = 0°$, then the projections of the end-effector's tip and body on {I} are collinear, and the tip points to either upward or downward directions. Here, we use symbols "Ua_m" and "Da_m" to discriminate these two directions, as shown in Fig. 3(b), where ten different orientations in 3-D are marked. The corresponding ten misalignment angles and the limit angles $\bar{a}$ in {I} are shown in Fig. 3(c).

Integrating the translational displacements to the model in (1), we can obtain the following general rotational model of end-effectors under microscopy:

$$\mathbf{P}_t = r\sin(\alpha_0 + p_r)\,(\mathbf{V}_n \times \mathbf{V}_a) + r\cos(\alpha_0 + p_r)\mathbf{V}_a + \mathbf{P}_c + \mathbf{P}_{xyz} \quad (2)$$

where $\mathbf{P}_{xyz}$ denotes the translational displacements along X_m, Y_m, and Z_m axes; p_r denotes the rotational displacement about the T_m axis; and α_0 denotes the initial rotation angle within the circle plane. Taking derivative of the model in (2) with respect to time t, we can eliminate $\mathbf{P}_c$ and obtain the following continuous-time model:

$$\begin{aligned} \dot{p}_x &= u_x + u_r r\,(\sin(\alpha_0 + p_r)\sin\varphi - \cos(\alpha_0 + p_r)\cos\varphi\sin\xi) \\ \dot{p}_y &= u_y - u_r r\,(\sin(\alpha_0 + p_r)\cos\varphi + \cos(\alpha_0 + p_r)\sin\varphi\sin\xi) \\ \dot{p}_z &= u_z + u_r r\cos(\alpha_0 + p_r)\cos\xi \\ \dot{p}_r &= u_r \end{aligned} \quad (3)$$

where u_x, u_y, u_z, and u_r denote the velocities of X_m, Y_m, Z_m, and T_m axes, respectively. The outputs of the system are considered as

$$y_x = \lambda_x p_x, y_y = \lambda_y p_y, y_z = p_z, y_r = a_m \quad (4)$$

where y_x and y_y denote coordinates of the end-effector's tip in {I}; λ_x and λ_y denote the ratio of pixel and displacement along X_m and Y_m axes, respectively; y_z denotes the displacement along the Z_m axis; and y_r denotes the misalignment angle a_m.

In fact, y_r can also be derived based on the model in (2) and the specifications of the end-effector, but it is not possible to obtain a general expression since y_r heavily depends on the geometric dimensioning of the end-effector or the concerned feature points on the end-effector. For instance, $\bar{a} \approx 33.7^\circ$ holds under $\xi = 30^\circ$, so we even cannot set a_m to 40° in this case. Thus, it is not significant to present the model-based equation of y_r. It should be underscored that the parameter vector $\mathbf{\Psi} := [r, \alpha_0, \varphi, \xi, p_{xc}, p_{yc}, p_{zc}]^{\mathrm{T}}$ updates every time when the end-effector is replaced.

Based on basic algebraic operations, the model in (3) can be rewritten to the following compact form, which is convenient for later controller design:

$$\dot{p}_x = u_x + u_r \sin p_r \delta_{x1} + u_r \cos p_r \delta_{x2} \tag{5}$$

$$\dot{p}_y = u_y - u_r \sin p_r \delta_{y1} - u_r \cos p_r \delta_{y2} \tag{6}$$

$$\dot{p}_z = u_z + u_r \cos p_r \delta_{z1} - u_r \sin p_r \delta_{z2} \tag{7}$$

$$\dot{p}_r = u_r \tag{8}$$

where

$$\delta_{x1} = r\sqrt{\sin^2\varphi + \cos^2\varphi \sin^2\xi}\cos(\alpha_0 - \tan^{-1}(\cot\varphi \sin\xi))$$

$$\delta_{x2} = r\sqrt{\sin^2\varphi + \cos^2\varphi \sin^2\xi}\sin(\alpha_0 - \tan^{-1}(\cot\varphi \sin\xi))$$

$$\delta_{y1} = r\sqrt{\cos^2\varphi + \sin^2\varphi \sin^2\xi}\cos(\alpha_0 + \tan^{-1}(\tan\varphi \sin\xi))$$

$$\delta_{y2} = r\sqrt{\cos^2\varphi + \sin^2\varphi \sin^2\xi}\sin(\alpha_0 + \tan^{-1}(\tan\varphi \sin\xi))$$

$$\delta_{z1} = r\cos\xi\cos\alpha_0, \delta_{z2} = r\cos\xi\sin\alpha_0.$$

IV. Visual Detection

The objective of developing visual detection algorithms is to directly obtain system outputs independent of model (3). This provides the feedback channel for the system, which can be used to eliminate the output error and attenuate the uncertain parameter vector $\mathbf{\Psi}$.

The outputs y_x and y_y can be determined by visually locating the end-effector's tip [22]; y_r can be computed by designing image processing methods targeted to the concerned structures, such as embryo yolk [23], membrane [24], and sperm [25]. These methods work well and only need a few updates from existing literatures for a given task under different imaging conditions. Thus, we will focus on measuring y_z in the rest of this section.

As in (4), y_z equals to p_z, but we cannot directly measure p_z in the vertical direction under an optical microscope. A class of promising methods for indirectly measuring p_z is to characterize the model of p_z and image sharpness offline, and develop an online visual algorithms to evaluate the image sharpness. According to this idea, a high number of autofocus techniques based on depth-from-defocus have been developed [26], [27]. However, this technique requires the object to have a fixed geometrical shape. This is not suitable for the rotational positioning problem since the end-effector constantly changes its postures during orientations. Another class of autofocus techniques does not characterize the model, but uses the gradient information of the captured images at different p_z positions, see [28] and [29], for examples. However, it is time-consuming to move the end-effector upward and downward for focus at each new orientation.

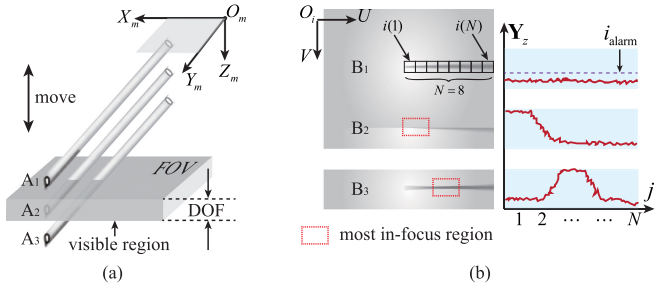

Fig. 4. Principle of the detection method within limited depth of field. (a) Three positional relationships (marked by A_1, A_2, and A_3) between the tilted end-effector and the microscope's limited visible region. (b) Images corresponding to the three cases in (a), marked by B_1, B_2, and B_3. $\mathbf{Y}_z$ is an update output vector to measure p_z which consists of N normalized values of image sharpness on N segments of the end-effector. i_{alarm} is an alarm lower bound of image sharpness in the focus loop in Section V.

To solve the autofocus problem during rotational positioning, we propose a detection method within limited DOF that can obtain the gradient information without moving the end-effector upward or downward. As illustrated in Fig. 4(a), the end-effector is commonly mounted at a tilted angle with one side down in micromanipulation, and the microscope has a limited FOV and DOF. We can classify the positional relationship between the end-effector and the microscope's visible region into three cases, as marked by A_1, A_2, and A_3. A_1 corresponds to the case where the end-effector is above the microscope visible region, so the image sharpness along the end-effector is low, as shown by B_1 in Fig. 4(b). On the other hand, if part of the end-effector enters the microscope's visible region, then that part becomes clear and the rest is blurry. A_2 and A_3 correspond to this case, and the most in-focus region is the end-effector's tip and partial body, as shown in B_2 and B_3. According to this observation, we define a new output vector $\mathbf{Y}_z$ to measure p_z as

$$\mathbf{Y}_z = [i(1), \ldots, i(N)]^{\mathrm{T}} = \frac{[I(1), \ldots I(N)]^{\mathrm{T}}}{\max(I(1), \ldots, I(N))} \tag{9}$$

where $I(\cdot)$ is a function to evaluate image sharpness, and $i(\cdot)$ is the normalized value. Commonly used functions of $I(\cdot)$ include squared gradient, normalized variance, entropy algorithm, as summarized in [30]. The input of $I(\cdot)$ is the image of the jth segment on the end-effector, $j \in [1, N]$, and N is the total number. For instance, $I(1)$ and $I(N)$ evaluate the image sharpness of the end-effector's tip and root, respectively; $i(1)$ and $i(N)$ are the normalized values.

The gradient information of image sharpness at different p_z is used for autofocus evaluation. In our method, two main reasons remove the commonly required back-and-forth movements of the end-effector. One reason is that the end-effector is always tilted; the other reason is that the depth of field of the optical microscope is limited. Under these conditions, only one image can provide sufficient image sharpness at different p_z positions. For a same misalignment angle a_m, the orientation of

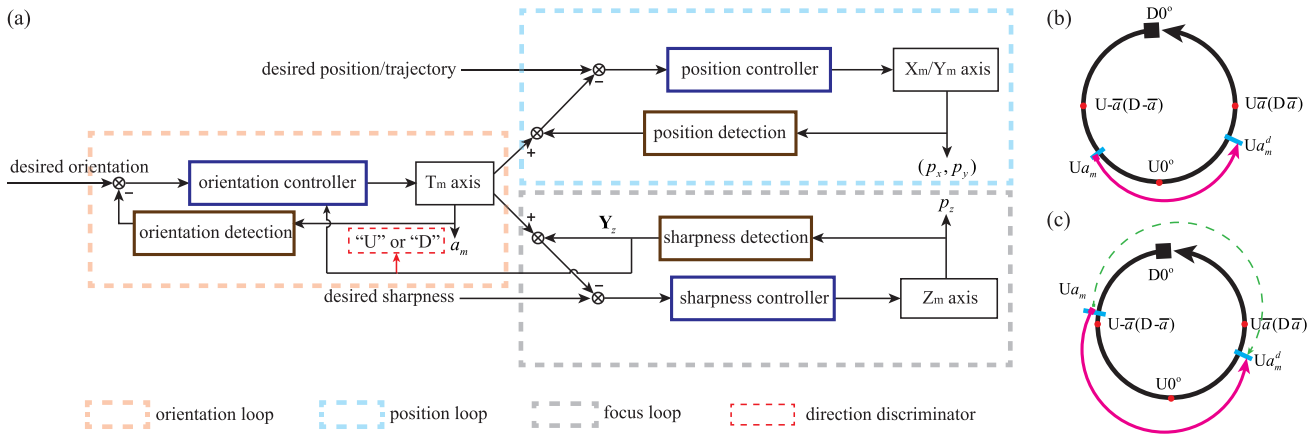

Fig. 5. Three-loop rotational control framework. (a) Orientation loop rotates about the T_m axis such that current orientation reaches the desired one. The position loop moves the X_m and Y_m axes to maintain the end-effector's tip (p_x, p_y) at the desired position or to trajectory. The focus loop keeps the end-effector within the microscope's depth of field for focus, and the range of $\mathbf{Y}_z$ discriminates the directions. In each loop, the detection and controller block diagrams can be replaced to concrete approaches to account for practical requirements. (b) Current and desired orientations (Ua_m and Ua_m^d, respectively) belong to the upward direction. A saturated proportional controller can rotate the end-effector to the desired orientation. (c) Current and desired orientations (Ua_m and Da_m^d, respectively) belong to different directions. A clockwise or counter clockwise rotation of the end-effector is determined with the purpose of minimizing the rotation angles before it turns to the case of (b).

"Ua_m" has a "smoother" $\mathbf{Y}_z$ than "Da_m" since more parts of the end-effector appear within the microscope's visible region. Here, we use the range of $\mathbf{Y}_z$, i.e., max($\mathbf{Y}_z$)–min($\mathbf{Y}_z$), as the metric to discriminate the upward and downward directions for a same a_m.

V. Three-Loop Rotational Control Framework

The requirements for rotational positioning control include the following:

1) maintaining the end-effector's tip [p_x and p_y in (5) and (6)] within the microscope's FOV;
2) keeping the end-effector's tip [p_z in (7)] within the microscope's depth of field; and
3) rotating the end-effector to a desired orientation [a_m in (4) with upward or downward directions].

In this section, a unified framework is designed with three loops, respectively, corresponding to the aforementioned three requirements, as shown in Fig. 5. This general control strategy is suitable for the end-effector alignment problem by setting the desired orientation in the orientation loop to U0° [6]. It can also be reduced to the case where a rotary stage is installed under microscopes by removing the focus loop [11], [20], [21]. Moreover, this control framework has the capability of *in situ* rotational positioning of the end-effector to different orientations, which is convenient for complex micromanipulation tasks, e.g., sperm orientation for aspiration (see Section VI-E).

The orientation loop steers the current orientation (denoted by $\phi_1 a_m$) to the desired one (denoted by $\phi_2 a_m^d$). ϕ_1 and ϕ_2 represent the end-effector's direction (upward or downward) and take values in $\{\mathrm{U}, \mathrm{D}\}$. The current orientation is visually detected depending on both the concerned features of the end-effector (for the value of a_m) and the range of $\mathbf{Y}_z$ (for the value of ϕ_1), which can be seen as a direction discriminator. The orientation controller is designed based on the rotational model and the orientation error. As illustrated in Section III, a_m is not involved in (3) as involving it breaks the generality of the derived results. Hence, the following error-based saturated controller is designed:

$$u_r = \begin{cases} \phi_1 = \phi_2 : \begin{cases} k_r\left(a_m^d - a_m\right), \left|k_r\left(a_m^d - a_m\right)\right| < \bar{u}_r \\ \operatorname{sgn}\left(k_r\left(a_m^d - a_m\right)\right)\bar{u}_r, \text{otherwise} \end{cases} \\ \phi_1 \neq \phi_2 : \begin{cases} \bar{u}_r, \left|a_m^d\right| < |a_m| \\ -\bar{u}_r, \left|a_m^d\right| \geq |a_m| \end{cases} \end{cases} \tag{10}$$

where sgn$(\cdot)$ is the sign function; $\bar{u}_r$ is the upper bound of u_r; and k_r is the proportional gain. According to (10), if $\phi_1 = \phi_2$ indicating that current and desired orientations have a same direction [see Fig. 5(b)], then a saturated proportional controller can effectively eliminate the orientation error; however, if $\phi_1 \neq \phi_2$ implying different directions, then the end-effector rotates at a constant velocity until $\phi_1 = \phi_2$, which turns into the first case. The rotational direction depends on $|a_m^d|$ and $|a_m|$, as shown in Fig. 5(c). The values of $|a_m|$ and $|a_m^d|$ can be seen as the distance to the nearest U0° or D0°. Hence, $|a_m^d| < |a_m|$ implies that counter clockwise rotation [the purple arrow in Fig. 5(c)] is smaller than clockwise rotation (the green dashed arrow). Thus, u_r is set to $\bar{u}_r$ in this case where "$-$" and "$+$" correspond to clockwise and counter clockwise directions, respectively. Additionally, rotation about the T_m axis also changes the position of the end-effector's tip (one input injected to the position loop) and the image sharpness of the end-effector's tip (another input injected to the focus loop).

The position loop maintains the end-effector's tip at a desired position or trajectory during orientation control. The values of p_x and p_y can be visually located [22], and the position controller is designed based on (5) and (6) and the output error. In micromanipulation and particularly the manipulation of biosamples, the end-effector needs to be frequently replaced due to contamination concerns. Therefore, the parameters in (5)

and (6) change after each replacement. To meet this practical requirement, a controller must be designed that work for a class of models with different parameters but described by a same structure. Here, we employ the adaptive robust controllers (adaptive to the model parameters and robust to the external disturbances) commonly used for servo control of nonlinear systems with uncertainties [31]–[33].

Define the positioning errors by $e_x := p_x - p_x^d$ and $e_y := p_y - p_y^d$, where p_x^d and p_y^d are desired values for p_x and p_y. We set p_x^d and p_y^d to the center of the microscope's FOV because the FOV center has a large distance to the FOV boundaries. Define $\hat{\delta}_{x1}$ and $\hat{\delta}_{x2}$ as the estimated values of δ_{x1} and δ_{x2} in (5), and let $\tilde{\delta}_{x1} = \hat{\delta}_{x1} - \delta_{x1}, \tilde{\delta}_{x2} = \hat{\delta}_{x2} - \delta_{x2}$ be the estimation error. Then, the adaptive robust controller is designed as

$$u_x = -k_x e_x - u_r \sin p_r \hat{\delta}_{x1} - u_r \cos p_r \hat{\delta}_{x2} + \frac{1}{\lambda_x} \dot{p}_x^d \quad (11)$$

with estimators

$$\begin{cases} \dot{\hat{\delta}}_{x1} = \text{Proj}_{\hat{\delta}_{x1}} \left(\lambda_x e_x u_r \sin p_r \right) \\ \dot{\hat{\delta}}_{x2} = \text{Proj}_{\hat{\delta}_{x1}} \left(\lambda_x e_x u_r \cos p_r \right) \end{cases}$$

where $\text{Proj}_{\hat{\delta}}(\tau)$ is defined by [34]

$$\text{Proj}_{\hat{\delta}} (\tau) = \begin{cases} 0, \text{ if } \begin{cases} \hat{\delta} = r \text{ and } \tau > 0 \\ \hat{\delta} = r \text{ and } \tau < 0 \end{cases} \\ \tau, \text{ otherwise} \end{cases}.$$

The asymptotic stability of the closed-loop servo system can be proved by establishing the Lyapunov function of the form $V_x := \frac{1}{2} e_x^2 + \frac{1}{2} \tilde{\delta}_{x1}^2 + \frac{1}{2} \tilde{\delta}_{x2}^2$. The proof is similar to our previous work [33] and, thus, omitted here. The other adaptive robust controller u_y of parameters k_y, $\hat{\delta}_{y1}$, and $\hat{\delta}_{y2}$ with similar structures to (11) can be applied to drive p_y to p_y^d, and is also omitted for simplicity.

Based on (7), an adaptive robust controller can also be designed in the focus loop. However, as stated in Section IV, p_z cannot be measured, and the precise relationship between p_z and image sharpness cannot be characterized. Thus, we update the output in this loop to $\mathbf{Y}_z$ in (9). To keep the end-effector's tip within the microscope's depth of field during orientations, the following proportional controller is developed according to the three cases in Fig. 4:

$$u_z = \begin{cases} k_z \left(i^d(1) - i(1) \right), \begin{cases} \text{B}_1 : \max \left(\mathbf{Y}_z \right) < i_{\text{alarm}} \\ \text{B}_2 : \text{pos} \left(\max \left(\mathbf{Y}_z \right) \right) = 1 \end{cases} \\ k_z \left(i(1) - i^d(1) \right), \begin{cases} \text{B}_3 : \max \left(\mathbf{Y}_z \right) > i_{\text{alarm}} \\ \text{pos} \left(\max \left(\mathbf{Y}_z \right) \right) \neq 1 \end{cases} \end{cases} \quad (12)$$

where k_z is the proportional gain; $i^d(1)$ is the desired image sharpness value of the end-effector's tip; i_{alarm} is an alarm lower bound of the image sharpness value of the end-effector's tip; and pos(max($\mathbf{Y}_z$)) is a function to return the index of the most in-focus region.

An analysis of the relationship between the derived conditions in (12) and the three cases B_1, B_2, and B_3 is made. B_1: $\max(\mathbf{Y}_z) < i_{\text{alarm}}$ indicates that the image sharpness on each segment of the end-effector is low; thus, the end-effector needs to move downward for focus. This is enabled since $i^d(1) - i(1) > 0$ holds in this case. B_2: $\text{pos}(\max(\mathbf{Y}_z)) = 1$ implies that the most in-focus region contains the micropipette tip; thus, the end-effector needs to move downward for further focus. B_3: $\text{pos}(\max(\mathbf{Y}_z)) \neq 1$ means that the most in-focus region is not the end-effector's tip, and the end-effector needs to move upward for focus. It seems that $\text{pos}(\max(\mathbf{Y}_z)) = 1$ and $\text{pos}(\max(\mathbf{Y}_z)) \neq 1$ contain all the possible cases. However, $\text{pos}(\max(\mathbf{Y}_z)) \neq 1$ may also hold under $\max(\mathbf{Y}_z) < i_{\text{alarm}}$ because in this case (B_1), elements of $\mathbf{Y}_z$ are low and close to each other. Therefore, we cannot definitively determine which segment is the most in-focus region.

It should be noted that other controllers can also be applied under the proposed unified three-loop control framework. For instance, sliding-mode control [35] or model predictive control [36] may also perform well in the position loop, due to their strong capabilities of resisting uncertainties and explicitly handling constraints. Additionally, extremum seeking approaches may be used in the focus loop [37].

VI. Experimental Results

Human sperm samples used in experiments were obtained from CReATe Fertility Centre (Toronto). The approval was obtained from Research Ethics Board of University of Toronto (application number UT35544).

A. Model Validation

To verify the validity of the proposed model in (2), we first identified the model parameters, and then rotated the end-effector about the T_m axis with translation compensation in open loop, to see whether the end-effector's tip was maintained at the initial position (i.e., the FOV center) and kept within the depth of field during 360° orientations. Parameters identification was conducted via an iterative procedure: rotating the end-effector about the T_m axis for a small angle, and moving the end-effector's tip back to the microscope's FOV center and the focal plane. The coordinates of X_m, Y_m, Z_m, and T_m axes were recorded for further identification. A least squares method was applied to fit the derived model in (2) by the recorded data.

As shown in Fig. 6(a), all the experimental data (i.e., the recorded data) were approximately located on a tilted circle in 3-D, and well fitted the model in (2). We also implemented the TIA approach [6] to identify the model parameters, but the resulting model yielded large errors in the tilted angle (ξ) and the radius (r). This is because when the end-effector's tip was far from the rotational axis, a very small rotation induced a large translation. Hence, having three points far enough from each other is a rather stringent requirement in the TIA approach, and the three points close to each other cannot capture sufficient characteristics of the model. For illustration, we also plotted a cube with the size of the microscope's FOV, 2.16 mm $\times$1.62 mm under a 4$\times$ objective. The height of the cube is 200μ m. Three images of the end-effector's tip captured within the cube were marked by M_1, M_2, and M_3 in Fig. 6, where the tip at the M_1 and M_3 positions was blurry.

We then rotated the end-effector about the T_m axis and compensated for the induced-translation by moving the X_m,

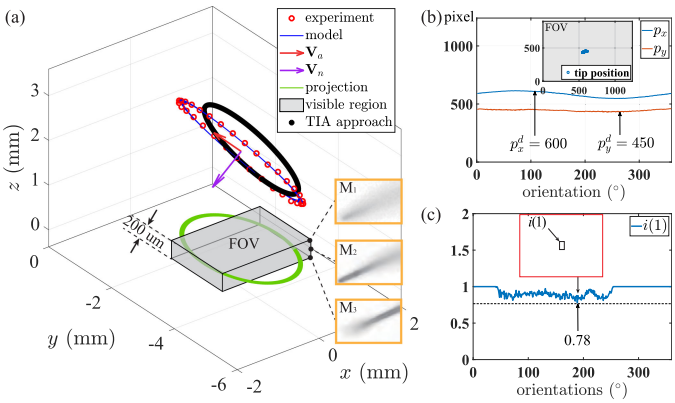

Fig. 6. Model validation. (a) Models were identified by experimental data and the TIA approach [6], and visualized by two circles in 3-D. (b) and (c) Positions (p_x and p_y) and image sharpness ($i(1)$) of the end-effector's tip in the microscope's FOV by 360° orientations and model-based translational compensation. Small positioning errors of p_x, p_y and large $i(1)$ verified the validity of the derived model.

TABLE I
MODEL PARAMETER VECTOR $\mathbf{\Psi}$ AFTER REPLACING THE END-EFFECTOR FIVE TIMES

$\mathbf{\Psi}\backslash\#$	1	2	3	4	5	average
r (mm)	1.6	1.1	1.2	1.5	1.6	1.4
α_0 (°)	50.5	0.7	−6.9	3.6	28.0	15.2
φ (°)	−0.5	2.0	1.2	0.9	−1.3	0.5
ξ (°)	37.4	39.2	39.1	38.7	37.5	38.4
p_{xc} (mm)	−5.1	−2.5	−4.2	−6.5	0.5	−3.6
p_{yc} (mm)	−2.8	−4.8	−4.8	−4.7	−2.9	−4
p_{zc} (mm)	1.8	−2.7	−0.4	−2.3	−0.8	−0.9

Y_m, and Z_m axes as derived by the identified model. As shown in Fig. 6(b), p_x and p_y were close to the microscope's FOV center during 360° orientations, and the ranges of p_x and p_y were as small as 68 and 32 pixels, compared to the image size of 1200 × 900 pixels. In Fig. 6(c), $i(1)$ has a small range during orientations (minimal value: 0.78), indicating that the end-effector's tip in the vertical direction was maintained within the microscope's depth of field. These results verified the validity of the identified model parameters.

Table I shows five groups of identified parameters in model (2) after replacing the end-effector five times. The values of $\mathbf{P}_c$ in the last three rows varied much; however, they were removed in the continuous-time model (3). The values of ξ and φ varied slightly around the end-effector's mounting angle (38°) and installation angle (0°). The value of α_0 indicates the initial position of the end-effector's tip within the tilted circle in 3-D; therefore, it can be any degree belonging to $[0, 360°]$. The circle's radius (r) changed much (range: 0.5 mm); thus, control methods based on the precise model without reidentification after end-effector replacement may result in the poor performance or even instability.

B. Performance Evaluation of Visual Detection

The performance of the proposed visual detection method for measuring p_z was evaluated. The algorithms for determining y_x, y_y, and y_r in (4) are not discussed here since they are similar to existing methods [22]–[24].

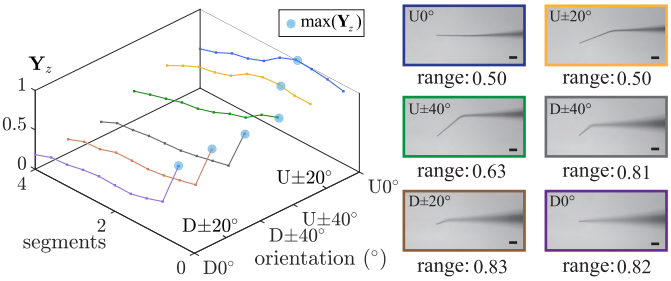

Fig. 7. Evaluation of the proposed detection method. $\mathbf{Y}_z$ captures the gradient information of image sharpness from one image. The range of $\mathbf{Y}_z$ can discriminate upward and downward directions for a same misalignment angle. "range" means the value of max($\mathbf{Y}_z$)–min($\mathbf{Y}_z$). Scale bar: 100 μm.

As discussed in Section III, the limit misalignment angle $\bar{a} \approx 40.5°$, i.e., $a_m \in [-40.5°, 40.5°]$. In the experiment, we selected ten orientations within this range to test the performance: U0°, U±20°, U±40°, D±40°, D±20°, and D0°, where U±40° and D±40° were very close to the limit misalignment angle. The function $I(\cdot)$ was selected as the normalized variance for evaluating image sharpness.

The value of $\mathbf{Y}_z$ was calculated according to (9) ($p > 0.05$, $n = 10$), and shown in Fig. 7. For downward directions, such as D0°, D±20°, D±40°, pos(max($\mathbf{Y}_z$)) was equal to 1. This indicates that the tip was in the most in-focus region and much clearer than the other segments of the end-effector. For the other three cases where the end-effector's tip pointed upward, the first several segments on the end-effector all had high image sharpness; thus, pos(max($\mathbf{Y}_z$)) was not equal to 1 for U0° and U±20°. According to (12), the end-effector moved upward for focus (B_3) until $\mathbf{Y}_z$ reached the condition in the B_2 case; then the end-effector moved downward until $\mathbf{Y}_z$ returned to the B_3 case. This feedback mechanism kept the end-effector's tip in the neighborhood of the microscope's depth of field. Thus, the design of $\mathbf{Y}_z$ can effectively measure the image sharpness along the end-effector and obtain the gradient information from only one image. It saves time cost without moving back-and-forth and meets the requirement of dynamic rotational positioning.

For U±40°, the range of $\mathbf{Y}_z$, i.e., max($\mathbf{Y}_z$)–min($\mathbf{Y}_z$), was 0.63 and increased significantly to 0.81 for D±40°. This result demonstrated that our method was also effective to discriminate the upward and downward directions with a same misalignment angle, even if they were very close to the limit misalignment angle.

This section presents the performance evaluation results of the proposed three-loop control framework. The evaluation metrics were selected as the values of p_x, p_y, $\mathbf{Y}_z$, and a_m, as labeled in Fig. 5. The final value of a_m was used to evaluate the orientation error. The average distance between (p_x, p_y) and microscope's FOV center during the whole orientation process (i.e., average positioning error) was used to characterize the position servo capability. $\mathbf{Y}_z$ was used to test the focus capability. Ten orientations (D0°, D±20°, D±40°, U±40°, U±20°, and U0°) were set as the desired orientations in the orientation loop. Before each experiment, the end-effector's tip was placed to the FOV center for a fair comparison with an arbitrarily initial orientation. All the experiments were performed under 4× and 20× objectives.

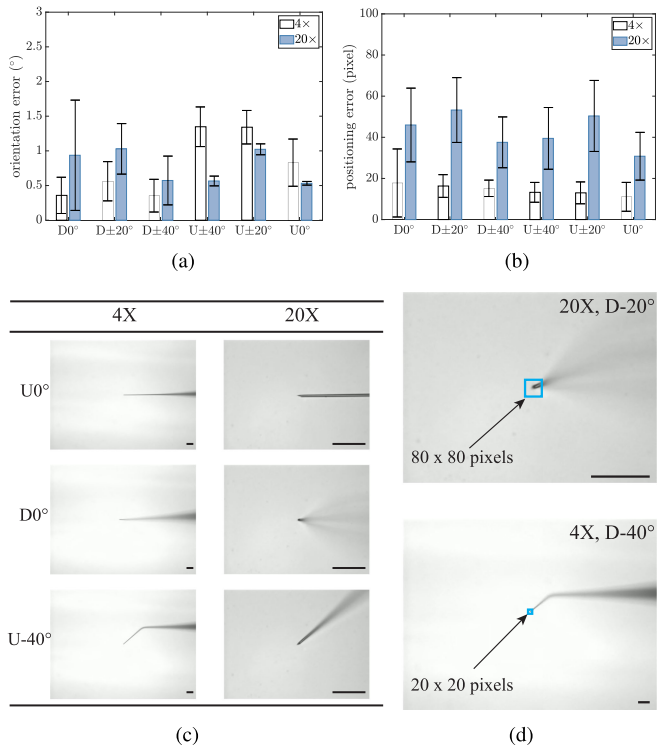

Fig. 8. Performance evaluation of rotational positioning control. Ten orientations, ranging from D 0° to U0°, were set as the desired orientations. (a) and (b) Orientation error and positioning error under 4× and 20× microscope objectives ($p > 0.05, n = 10$). (c) and (d) Microscope FOV images after robotic orientation to desired values. Scale bar: 100 μm.

Fig. 8(a) shows the orientation errors for the ten desired orientations under two magnifications. The average errors were less than 2° for all the cases. Moreover, the average errors under 20× objective were smaller than 4× objective for upward directions (U±40°, U±20°, and U0°), but were larger for downward directions (D±40°, D±20°, and D0°). This is because higher magnifications provided more details for calculating the misalignment angle for upward directions [see U0° and U−40° in Fig. 8(c)], but the end-effector under high magnifications also became more blurry for downward directions due to the more limited depth of field, which also resulted in large variances of orientation error [D0° in Fig. 8(c)].

The end-effector's alignment (i.e., aligning the tip to the micropipette body) is a basic requirement in micromanipulation. This operation is presently manually conducted and can easily cause damage to the fragile end-effectors. The alignment problem is a particular case of our proposed rotational positioning (U0°). In our experiments, a smaller average orientation error with a lower standard deviation was achieved under 20× than under 4× [0.5° versus 0.7° for U0° in Fig. 8(a)].

Fig. 8(b) shows the positioning error of the end-effector's tip during orientations. The positioning error was defined by the distance between the end-effector's tip and the FOV center during the whole orientation process, and the error was visualized by a square with the side length of the error value [see Fig. 8(d)]. Under 4× and 20× objectives, the average positioning error was less than 20 pixels (36 μm) and 80 pixels (29 μm), respectively, where the area ratios of the error square and the microscope's FOV were 0.6% and 0.04% ($p > 0.05$, $n = 10$). These errors were significantly smaller than those by manual operation.

TABLE II
SIX GROUPS OF CONTROL GAINS FOR COMPARISON

gains\#	1	2	3	4	5	6
k_x, k_y	**10**	**100**	100	100	100	100
$k_r/\bar{u}_r$	10/100	10/100	**10/100**	**10/500**	10/100	10/100
k_z	200	200	200	200	**50**	**500**

#1 and #2 are for position loop; #3 and #4 are for orientation loop; and #5 and #6 are for focus loop.

TABLE III
EVALUATION METRICS FOR THREE CONTROL LOOPS UNDER DIFFERENT CONTROL GAINS

	position loop	orientation loop	focus loop
metrics	pos. error	pos. error and time cost	ave./max. of $i(1)$
#	1,2	3,4	5,6
results	226.3, 35.2	35.9 (21), 136.4 (11)	36%,63%

The metric in #1 and #2 is positioning error (i.e., distance between end-effector's tip and FOV center during orientations, unit: pixel). Metrics in #3 and #4 include positioning error (unit: pixel) and time cost (unit: s). The metric in #5 and #6 is the ratio of average and maximal values of $i(1)$. The indices 1 to 6 correspond to the control gains in Table II.

We also tested the control performance under different k_x, k_y, k_z, and $k_r(\bar{u}_r)$ in controllers (10)–(12) (see Supplementary Video). As shown in Table II, six groups of control gains including k_x, k_y, k_r, $\bar{u}_r$, and k_z were assigned to the controllers in the three loops. Table III summarizes the resulting control performance. In the experiment, the desired orientation was set to U0°. In the first test, the values of k_x, k_y in the position loop were set to 10 in #1, and 100 in #2. The positioning errors for the two cases were 226.3 and 35.2 pixels, indicating that large k_x and k_y can improve the servo capability. In the second test, the values of k_r and $\bar{u}_r$ in the orientation loop were set to 10 and 100 in #3, and 10 and 500 in #4. The positioning errors were 35.9 and 136.4 pixels. Although large $\bar{u}_r$ resulted in large errors, it also achieved significantly faster alignment (11 s versus 21 s). In the third test, the value of k_z in the focus loop was set to 50 in #5 and 500 in #6. The average (and the maximal) values of $i(1)$ during orientations were measured to be 12 (34) and 22 (35). The ratio of the average and maximal values of $i(1)$ was 36% and 63%, respectively, indicating that the end-effector in #5 was much further from the focal plane than #6, and large k_z can yield a better focus capability.

C. Robotic Sperm Immobilization

We applied the derived rotational positioning control approach to micropipette alignment, which was a prerequisite for sperm immobilization. Human sperm samples in the experiments were obtained from CReATe Fertility Centre (Toronto) and informed consent was obtained from the subjects.

Since a smaller orientation error at U0° can be achieved under a high magnification [see Fig. 8(a)], the micropipette was aligned under 4× and realigned under 20× [see Fig. 9(a)]. After the human operator selected a swimming sperm via computer mouse clicking, the micropipette was moved to be above the sperm tail and tapped the substrate to immobilize the sperm. Sperm immobilization was considered successful if the sperm lost its motility [see Fig. 9(b)]. However, when there was a misalignment error such as U-4.1° [see Fig. 9(c)], a gap existed

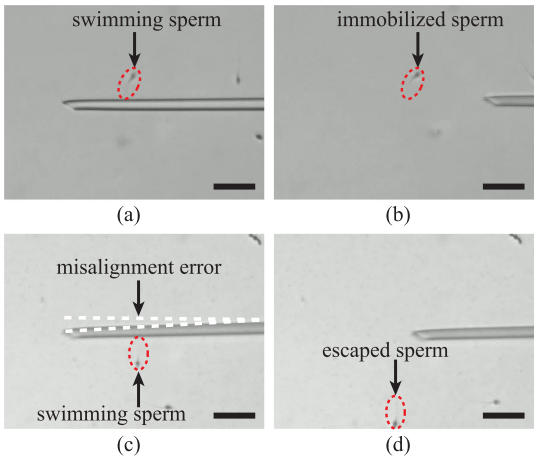

Fig. 9. Sperm immobilization. (a) Robotic micropipette alignment. (b) Immobilized sperm. (c) Manual micropipette alignment resulted in a misalignment error and a gap between micropipette and substrate. (d) Sperm escaped. Scale bar: 25 μm.

TABLE IV
AVERAGE ORIENTATION ERROR, TIME COST, AND SUCCESS RATE OF SPERM IMMOBILIZATION BY THREE TYPES OF MICROPIPETTE ALIGNMENT: ROBOTIC ALIGNMENT UNDER 4×, MANUAL ALIGNMENT, AND ROBOTIC REALIGNMENT UNDER 20×

	alignment (4×)	manual	re-alignment (20×)
orientation error (°)	0.7	3.6	0.5
time cost (s)	8.2	13.8	20.5
success rate (%)	97	90	98

(Total number of sperm: 300).

between the micropipette and the substrate, through which the sperm could escape, resulting in immobilization failure [see Fig. 9(d)].

Robotic sperm immobilization was conducted on 300 sperm by three types of micropipette alignment (100 sperms in each type). The first and second types were robotic and manual alignment under 4×, and the third type was realignment under 20× after the first two types. The third type can be seen as a coarse-to-fine operation of micropipette alignment under a higher magnification, which is difficult to achieve by human operation due to the very limited FOV.

Table IV shows the average orientation error, time cost, and success rate of sperm immobilization by these three types of micropipette alignment. The initial misalignment error was adjusted to be U-20° in each experiment for a fair comparison. Realignment under 20× achieved the smallest orientation error (0.5°) because more micropipette details were captured under a high magnification; however, the time cost of 20.5 s was much higher than that by robotic alignment (8.2 s) and manual alignment (13.8 s) under 4×. Although the success rate of sperm immobilization by robotic realignment under 20× (98%) was only slightly higher than that by robotic alignment (97%) under 4×, it was significantly higher than that by manual operation (90%). In summary, robotic alignment under 4× increased the success rate and improved the efficiency of sperm immobilization, and robotic realignment under 20× provided a higher success rate at the expense of higher time cost.

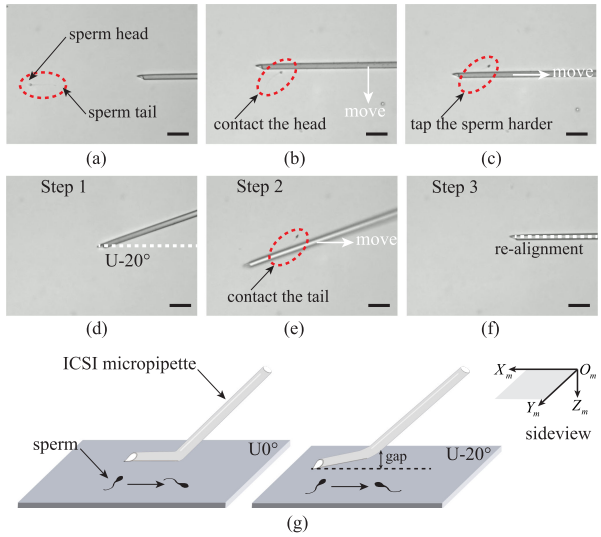

Fig. 10. Sperm orientation for aspiration. (a) Sperm tail must be aligned to the micropipette tip before aspiration. (b) and (c) Sperm tail cannot be aligned to the micropipette at U0°. (d)–(f) Three steps that align sperm tail to the micropipette tip by dynamically rotating the micropipette to different orientations. (g) Side view of micropipette at U0° and U-20°. In the case of U0°, no gap existed between the micropipette and substrate; hence, any movement along the Y_m axis aligned sperm head (b), and any movement along the X_m axis tapped the sperm hard, which cannot exert sufficient forces to orient the sperm (c); in the case of U-20°, a gap existed so that the micropipette can contact the sperm tail without tapping the sperm hard. Scale bar: 25 μm.

D. Robotic Sperm Orientation for Aspiration

In clinical ICSI, an immobilized sperm needs to be aspirated into the micropipette for deposition into an oocyte. As a clinical requirement, the sperm tail must be aligned to the micropipette tip before aspiration so that the sperm head is first-out during deposition [see Fig. 10(a)]. In the sperm orientation process, since sperm DNA is all contained in the head, damage to sperm head must be avoided. Under these requirements, a sperm with its head very close to the micropipette is difficult to be aligned because the movement of the micropipette along the Y_m axis makes the micropipette tip contact the sperm head first, and eventually aligns the sperm head to the micropipette [see Fig. 10(b)]. On the other hand, if the micropipette is lifted, is moved to be above the sperm tail, and directly contacts the tail, then the movement of the micropipette along the X_m axis would tap the sperm tail harder, without being able to exert sufficient forces to orient the sperm [see Fig. 10(c)]. For this difficult case, clinical operators often use the micropipette to slide the culture medium rapidly by trial and error until the sperm tail is aligned to the micropipette. However, this operation is laborious, time-consuming, and may damage the fragile micropipette.

To address this sperm orientation challenge, we developed a method consisting of three steps by dynamically rotating the micropipette to different orientations [see Fig. 10(d)–(f)]. In the first step, the micropipette was intentionally rotated to generate a small misalignment error, such as U-20° [see Fig. 10(d)]. This operation yielded a gap between the micropipette and the substrate. Then, the micropipette was controlled to contact the sperm tail and move along the X_m axis until the sperm

tail was well aligned [see Fig. 10(e)]. At this orientation, the micropipette tip was able to rotate the sperm without tapping the sperm tail hard because the gap accommodated the sperm. The micropipette tip was then realigned to U0° for sperm aspiration [see Fig. 10(f)]. Fig. 10(g) shows the side view of the micropipette tip at U0° and U-20°. Note that U0° was not suitable for sperm orientation, and U-20° was inconvenient for sperm immobilization and aspiration. Instead of relying on a fixed orientation of the micropipette, these tasks were well addressed by the versatility of *in situ* orientation control.

E. Discussion

Based on the experimental results, several guidelines can be given to implement the proposed rotational positioning technique in other applications. First, visual detection and control methods in each control loop can be revised. For instance, model predictive control may be more appropriate for manipulation under high magnifications, since it can absolutely constrain the end-effector within the FOV at the expense of high online computational burden. Second, one can further reduce the orientation error from the following three aspects.

1) The orientation detection accuracy can be improved by developing more targeted algorithms.
2) Mechanical vibration can be attenuated by replacing the hollow shaft stepper motor to a high-performance direct current motor.
3) Dual-mode control [36] can be introduced to reduce motor vibration in the neighborhood of the desired orientation.

Third, collision detection is necessary in practical applications, which can be achieved by using contact detection methods [38]. The concept of contact detection is to visually sense the abrupt changes in the motion pattern upon the contact between the end-effector and substrate. Additionally, relatively small controller gains are recommended to avoid collision of the end-effector with the environment, for instance, a small $\bar{u}_r$ in (10) can lower the rotational velocity and, thus, reduce the requirement of the bandwidth in the position loop and the focus loop.

VII. Conclusion

This article reported a rotational positioning method of end-effectors under microscopy for micromanipulation. The general and practical conditions considered include: the rotational axis of the end-effector is at a tilted angle to the microscope's focal plane, and the end-effector's tip is far from the rotational axis. We also considered other practical requirements, such as frequent replacement of the end-effectors and the very limited microscope's FOV. A general rotational model was established, which can be reduced to other rotational models in the literature. A detection method within limited depth of field was developed to determine the focus direction based on only one image. A unified three-loop rotational positioning control framework was proposed, which covers existing control methods as particular cases. Experimental results demonstrated that the proposed method was able to rotate the end-effector's tip to an arbitrarily desired orientation with an average orientation error less than 2°. This small orientation error improved the success rate of sperm immobilization (≥97%), which was significantly higher than the success rate achieved by manual orientation (90%). The approach also enables versatile *in situ* control for orienting the end-effector to multiple desired orientations.

References

[1] P. Rubino, P. Viganò, A. Luddi, and P. Piomboni, "The ICSI procedure from past to future: A systematic review of the more controversial aspects," *Hum. Reprod. Update*, vol. 22, no. 2, pp. 194–227, 2016.

[2] K. Koos *et al.*, "Automatic deep learning-driven label-free image-guided patch clamp system," *Nature Commun.*, vol. 12, 2021, Art. no. 936, doi: 10.1038/s41467-021-21291-4.

[3] Z. Liu *et al.*, "Cloning of macaque monkeys by somatic cell nuclear transfer," *Cell*, vol. 172, no. 4, pp. 881–887, 2018.

[4] F. Berndt, G. Shah, R. M. Power, J. Brugués, and J. Huisken, "Dynamic and non-contact 3D sample rotation for microscopy," *Nature Commun.*, vol. 9, 2018, Art. no. 5025, doi: 10.1038/s41467-018-07504-3.

[5] Z. Lu, X. Zhang, C. Leung, N. Esfandiari, R. Casper, and Y. Sun, "Robotic ICSI (intracytoplasmic sperm injection)," *IEEE Trans. Biomed. Eng.*, vol. 58, no. 7, pp. 2102–2108, Jul. 2011.

[6] Y. Shen, W. Wan, H. Lu, T. Fukuda, and W. Shang, "Automatic sample alignment under microscopy for 360° imaging based on the nanorobotic manipulation system," *IEEE Trans. Robot.*, vol. 33, no. 1, pp. 220–226, Feb. 2017.

[7] H. Lu, Y. Yang, X. Lin, P. Shi, and Y. Shen, "Low-invasive cell injection based on rotational microrobot," *Adv. Biosyst.*, vol. 3, no. 7, 2019, Art. no. 1800274.

[8] X. Liu, K. Kim, Y. Zhang, and Y. Sun, "Nanonewton force sensing and control in microrobotic cell manipulation," *Int. J. Robot. Res.*, vol. 28, no. 8, pp. 1065–1076, 2009.

[9] K. Inoue, Y. Matsuzaki, and S. Lee, "Micromanipulation using micro hand with two rotational fingers," *J. Micro-Nano Mech.*, vol. 7, pp. 33–44, 2012.

[10] C. Pardo-Martin, A. Allalou, J. Medina, P. M. Eimon, C. Wählby, and M. F. Yanik, "High-throughput hyperdimensional vertebrate phenotyping," *Nature Commun.*, vol. 4, 2013, Art. no. 1467, doi: 10.1038/ncomms2475.

[11] Z. Wang, W. T. Latt, S. Y. M. Tan, and W. T. Ang, "Visual servoed three-dimensional cell rotation system," *IEEE Trans. Biomed. Eng.*, vol. 62, no. 10, pp. 2498–2507, Oct. 2015.

[12] Y. Wen, H. Lu, Y. Shen, and H. Xie, "Nanorobotic manipulation system for 360° characterization atomic force microscopy," *IEEE Trans. Ind. Electron.*, vol. 67, no. 4, pp. 2916–2924, Apr. 2020.

[13] K. Mani, T.-C. C. Chien, B. Panigrahi, and C.-Y. Chen, "Manipulation of zebrafish's orientation using artificial cilia in a microchannel with actively adaptive wall design," *Sci. Rep.*, vol. 6, 2016, Art. no. 36385, doi: 10.1038/srep36385.

[14] Y. Zhang, K. K. Tan, and S. Huang, "Visual-servo system for automated cell injection," *IEEE Trans. Ind. Electron.*, vol. 56, no. 1, pp. 231–238, Jan. 2009.

[15] Y. Zhang, C. K. Brandon, X. Liu, and Y. Sun, "Autonomous robotic pick-and-place of microobjects," *IEEE Trans. Robot.*, vol. 26, no. 1, pp. 200–207, Feb. 2010.

[16] E. Avci *et al.*, "High-speed automated manipulation of microobjects using a two-fingered microhand," *IEEE/ASME Trans. Mechatron.*, vol. 62, no. 2, pp. 1070–1079, Feb. 2015.

[17] C. Dai *et al.*, "Robotic manipulation of deformable cells for orientation control," *IEEE Trans. Robot.*, vol. 36, no. 1, pp. 271–283, Feb. 2020.

[18] H. Lu, W. Shang, H. Xie, and Y. Shen, "Ultrahigh-precision rotational positioning under a microscope: Nanorobotic system, modeling, control, and applications," *IEEE Trans. Robot.*, vol. 34, no. 2, pp. 497–507, Apr. 2018.

[19] S. Zhuang, W. Lin, G. Zhang, J. Qiu, and H. Gao, "Visual servoed three-dimensional rotation control in zebrafish larva heart microinjection system," *IEEE Trans. Biomed. Eng.*, vol. 65, no. 1, pp. 64–73, Jan. 2018.

[20] X. Liu, Z. Lu, and Y. Sun, "Orientation control of biological cells under inverted microscopy," *IEEE/ASME Trans. Mechatron.*, vol. 16, no. 2, pp. 277–287, Oct. 2011.

[21] Z. Zhang *et al.*, "Robotic immobilization of motile sperm for clinical intracytoplasmic sperm injection," *IEEE Trans. Biomed. Eng.*, vol. 66, no. 2, pp. 444–452, Feb. 2019.

[22] J. Liu *et al.*, "Locating end-effector tips in robotic micromanipulation," *IEEE Trans. Robot.*, vol. 30, no. 1, pp. 125–130, Feb. 2014.

[23] W. Wang, X. Liu, and Y. Sun, "High-throuput automated injection of individual biological cells," *IEEE Trans. Autom. Sci. Eng.*, vol. 6, no. 2, pp. 209–219, Apr. 2009.

[24] H. Huang, D. Sun, J. Mills, and S. Cheng, "Robotic cell injection system with position and force control: Toward automatic batch biomanipulation," *IEEE Trans. Robot.*, vol. 25, no. 3, pp. 727–737, Jun. 2009.
[25] C. Dai *et al.*, "Automated non-invasive measurement of single sperm's motility and morphology," *IEEE Trans. Med. Imag.*, vol. 37, no. 10, pp. 2257–2265, Oct. 2018.
[26] A. P. Pentland, "A new sense for depth of field," *IEEE Trans. Pattern Anal. Mach. Intell.*, vol. 9, no. 4, pp. 523–531, Jul. 1987.
[27] M. Subbarao and N. Gurumoorthy, "Depth recovery from blurred edges," in *Proc. Comput. Soc. Conf. Comput. Vis. Pattern Recognit.*, 1988, pp. 498–503.
[28] Y. Yao, B. R. Abidi, and M. A. Abidi, "Extreme zoom surveillance: System design and image restoration," *J. Multimedia*, vol. 2, no. 1, pp. 20–31, 2007.
[29] S. Y. Lee, Y. Kumar, J. M. Cho, S. W. Lee, and S. W. Kim, "Enhanced autofocus algorithm using robust focus measure and fuzzy reasoning," *IEEE Trans. Circuits Syst. Video Technol.*, vol. 18, no. 9, pp. 1237–1246, Sep. 2008.
[30] Y. Sun, S. Duthaler, and B. J. Nelson, "Autofocusing algorithm selection in computer microscopy," in *Proc. IEEE/RSJ Int. Conf. Intell. Robots Syst.*, 2005, pp. 70–76.
[31] W. Sun, S. Tang, H. Gao, and J. Zhao, "Two time-scale tracking control of nonholonomic wheeled mobile robots," *IEEE Trans. Control Syst. Technol.*, vol. 25, no. 6, pp. 2059–2069, Nov. 2016.
[32] W. Sun, Y. Liu, and H. Gao, "Constrained sampled-data ARC for a class of cascaded nonlinear systems with applications to motor-servo systems," *IEEE Trans. Ind. Informat.*, vol. 15, no. 2, pp. 766–776, Feb. 2019.
[33] G. Zhang *et al.*, "Zebrafish larva orientation and smooth aspiration control for microinjection," *IEEE Trans. Biomed. Eng.*, vol. 68, no. 1, pp. 47–55, Jan. 2021.
[34] B. Yao and M. Tomizuka, "Adaptive robust control of MIMO nonlinear systems in semi-strict feedback forms," *Automatica*, vol. 37, no. 9, pp. 1305–1321, 2001.
[35] Q. Xu, "Adaptive discrete-time sliding mode impedance control of a piezoelectric microgripper," *IEEE Trans. Robot.*, vol. 29, no. 3, pp. 663–673, Jun. 2013.
[36] K. Zhang and Y. Shi, "Adaptive model predictive control for a class of constrained linear systems with parametric uncertainties," *Automatica*, vol. 117, no. 108974, pp. 1–8, 2020.
[37] L. Wang, S. Chen, and K. Ma, "On stability and application of extremum seeking control without steady-state oscillation," *Automatica*, vol. 68, pp. 18–26, 2016.
[38] W. Wang, X. Liu, and Y. Sun, "Contact detection in microrobotic manipulation," *Int. J. Robot. Res.*, vol. 26, no. 8, pp. 821–828, 2007.

Songlin Zhuang (Member, IEEE) received the B.E. degree in automation and the Ph.D. degree in control science and engineering from the Harbin Institute of Technology, Harbin, China, in 2014 and 2019, respectively.

From 2019 to 2020, he was a Postdoctoral Researcher with the Department of Mechanical and Industrial Engineering, University of Toronto, Toronto, ON, Canada. Since October 2020, he has been a Postdoctoral Fellow with the Department of Mechanical Engineering, University of Victoria, Victoria, BC, Canada. His research interests include control theory for industrial applications and robotic micromanipulation for biomedical applications.

Changsheng Dai (Member, IEEE) received the B.E. and M.E. degrees in mechanical engineering from the Harbin Institute of Technology, Harbin, China, in 2014 and 2016, respectively, and the Ph.D. degree in mechanical engineering from University of Toronto, Toronto, ON, Canada, in 2020.

He is currently working as a Postdoctoral Fellow with the Advanced Micro and Nanosystems Laboratory, University of Toronto. His research interests include robotic cell manipulation and medical robotics.

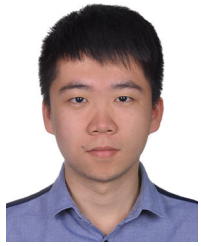

Guanqiao Shan (Graduate Student Member, IEEE) received the B.E. degree in electronic information and the M.S. degree in physics from Beihang University, Beijing, China, in 2014 and 2017, respectively. He is currently working toward the Ph.D. degree in mechanical engineering with the University of Toronto, Toronto, ON, USA.

His research interests include robotic cell manipulation and characterization.

Changhai Ru received the Ph.D. degree in mechatronics engineering from the Harbin Institute of Technology, Harbin, China, in 2005.

He was a Postdoctoral Fellow with the Department of Mechanical and Industrial Engineering, University of Toronto, Toronto, ON, Canada. He is currently a Professor with the School of Electronic and Information Engineering, Suzhou University of Science and Technology, Suzhou, China, and a Director of JITRI Micro-Nano Automation System and Equipment Technology Research Institute. His research areas include microrobotics and nanorobotic manipulation, nanopositioning technology, and automated instrumentation for biomedical applications.

Zhuoran Zhang (Member, IEEE) received the B.E. degree in automation from the Harbin Institute of Technology, Harbin, China, in 2014 and the Ph.D. degree in mechanical engineering from the University of Toronto, Toronto, ON, Canada, in 2019.

He is currently an Assistant Professor with the Chinese University of Hong Kong, Shenzhen, China. His research interests include robotic cell manipulation, automation at micronano scales, and medical robotics.

Yu Sun (Fellow, IEEE) received the B.S. degree in electrical engineering from the Dalian University of Technology, Dalian, China, in 1996, the M.S. degree in control system and robotics from the Institute of Automation, Chinese Academy of Sciences, Beijing, China, in 1999, and the M.S. degree in electrical engineering and the Ph.D. degree in mechanical engineering from the University of Minnesota, Minneapolis, MN, USA, in 2001 and 2003, respectively.

He is currently a Professor with the University of Toronto, Toronto, ON, Canada. He is currently a Tier I Canada Research Chair and the Director of the Robotics Institute, Pittsburgh, PA, USA. His lab specializes in developing innovative technologies and instruments for manipulating and characterizing cells, molecules, and nanomaterials.

Dr. Sun was elected Fellow of ASME (American Society of Mechanical Engineers), IEEE (Institute of Electrical and Electronics Engineers), AAAS (American Association for the Advancement of Science), NAI (National Academy of Inventors), CAE (Canadian Academy of Engineering), and RSC (Royal Society of Canada) for his work on micronano devices and robotic systems.